Non-Boltzmann Luminescence in $NaYF_4$:Eu^{3+}: Implications for Luminescence Thermometry

Robin G. Geitenbeek, Harold W. de Wijn, and Andries Meijerink*
Condensed Matter and Interfaces, Debye Institute for Nanomaterials Science, Utrecht University, Princetonplein 1, 3584 CC Utrecht, Netherlands

(Received 14 July 2018; revised manuscript received 17 September 2018; published 4 December 2018)

Luminescence (nano)thermometry is an important technique for remote temperature sensing. The recent development of lanthanide-doped nanoparticles with temperature-dependent emission has expanded the field of applications, especially for ratiometric methods relying on the temperature variation of relative emission intensities from thermally coupled energy levels. Analysis and calibration of the temperature dependence is based on a Boltzmann equilibrium for the coupled levels. To investigate the validity of this assumption, we analyze and model thermal equilibration for Eu^{3+} $^5D_1$ and $^5D_0$ emission in $NaYF_4$. The results show that for low Eu^{3+} concentrations, temperature-dependent multiphonon relaxation can accurately explain both the intensity ratio and emission decay dynamics. The analysis also reveals that a Boltzmann equilibrium is not realized in the temperature regime investigated (300–900 K). By increasing the Eu^{3+} concentration, cross relaxation between neighboring Eu^{3+} ions enhances $^5D_1$–$^5D_0$ relaxation rates and extends the temperature range in which emission intensity ratios can be used for temperature sensing (500–900+ K). The results obtained are important for recognizing, understanding, and controlling deviations from Boltzmann behavior in luminescence (nano)thermometry. By varying the dopant concentration, the range for accurate temperature sensing can be adjusted. These insights are crucial in the development and understanding of reliable temperature sensors.

DOI: 10.1103/PhysRevApplied.10.064006

I. INTRODUCTION

Luminescence thermometry [1–4] is a powerful tool for remote temperature sensing. Potential applications range from bio-imaging [5–9] at lower temperatures (<350 K) to nano-electronics [10,11] and chemical reactors [12–15] at elevated temperatures (up to 1500 K). In recent years, nanothermometry using luminescent nanoparticles has become an active field of research as this technique offers excellent spatial and temporal resolution for remote temperature sensing with high accuracy. Methods based on monitoring the intensity ratio between two or more emission peaks to determine the temperature are especially widely used [16]. The ratio is not affected by fluctuations of the overall intensity, e.g., by changes in alignment, light absorption, and scattering, or the concentration of luminescent species. Changes in the intensity ratio may arise from the temperature dependence of a variety of processes such as energy transfer between luminescent ions and relaxation rates between levels. In many cases, the fluorescence intensity ratio (FIR) changes with temperature as it is determined by the thermal population of two thermally coupled excited states separated by an energy difference ΔE. If ΔE is of the order of several kT, emission can be observed from both levels. The intensity of the emission is proportional to the population and as the temperature is raised the relative intensity of emission from the higher energy level will increase.

In the analysis of the intensity ratio, it is commonly assumed that the population of the two states follows a Boltzmann distribution [17]. The temperature regime in which the ratiometric thermometry has the highest accuracy is related to ΔE. The higher the temperature regime of interest, the larger ΔE should be. Depending on the application, temperature range, and sensitivity that are required, luminescent probes with different values for ΔE must be selected. A necessary condition for reaching Boltzmann equilibrium, however, is that equilibration of two thermally coupled states is fast in comparison with other processes affecting their population, notably optical feeding and decay channels to the ground state. For larger ΔE, relaxation between thermally coupled levels becomes slower, so that deviations from Boltzmann equilibrium tend to occur. In the common analysis of the temperature dependence of the intensity ratio, it is not always

*A.Meijerink@uu.nl

recognized that the population does not follow Boltzmann equilibrium and deviations from calibration curves are sometimes misinterpreted [18–20].

We analyze deviations from Boltzmann equilibrium for lanthanide-based temperature sensors which are among the most widely used ratiometric temperature probes. Our prototypal example will be $NaYF_4$:Eu^{3+}. Deviations from Boltzmann equilibrium affect the temperature range that can be probed. We furthermore show how the temperature range can be extended by inducing additional relaxation paths, namely by cross-relaxation interaction between lanthanide (Ln) ions at higher Ln-doping concentrations. Insight into the validity of the Boltzmann equilibrium is crucial in the application of ratiometric (nano)thermometry.

In a broader sense, Ln dopants in inorganic host materials are ideal for ratiometric (or bandshape) thermometry. The partly filled inner $4f$ shell of Ln ions gives rise to a large number of closely spaced energy levels [21]. Efficient sharp-line emissions can be observed in various spectral regions (IR, visible, and UV) for different Ln^{3+} ions. Many of the energy levels from which emission is observed have additional levels at higher energies, which are exploited for luminescence thermometry. The sharp-line emission from different closely spaced levels can be easily observed and separated, which allows for a highly accurate determination of intensity ratios. Advantages of Ln-doped inorganic host materials over other optical probes (e.g., quantum dots [22] or organic complexes [23]) are the high quenching temperature of emission [24,25], thermal stability of the material, and the insensitivity of the optical properties to variations in the environment (such as pH, embedding medium or solvent, pressure, etc.). For bio-imaging and other applications in the temperature range 300–600 K, Er^{3+} is a popular probe [26–28]. The $^4S_{3/2}$ and $^2H_{11/2}$ levels of Er^{3+} are separated by approximately 700 cm^{-1} and efficient green emission is observed from these levels. At temperatures above 600 K, deviations from the Boltzmann equilibrium for the $^4S_{3/2}$ and $^2H_{11/2}$ levels were observed [17], probably as a result of thermal population of even higher levels [29] (e.g., $^4F_{7/2}$). Dy^{3+} and Eu^{3+} with larger energy gaps (1100 cm^{-1} for the $^4F_{9/2}$–$^4I_{15/2}$ gap for Dy^{3+} and 1800 cm^{-1} for the $^5D_0$–$^5D_1$ gap for Eu^{3+}) are promising candidates for ratiometric thermometry at higher temperatures [30,31]. At present there is, however, a lack of understanding on how deviations from Boltzmann equilibrium and cross-relaxation processes affect the thermal response of Ln-based ratiometric temperature sensors.

Here, we consider in detail the temperature-dependent Eu^{3+} emission in microcrystalline $NaYF_4$ [32,33] and investigate the temperature range in which a Boltzmann equilibrium is established. Emission from the thermally coupled $^5D_0$ and $^5D_1$ states is measured and analyzed for a low-dopant concentration (0.4% Eu^{3+}) by using models for the temperature dependence of multiphonon relaxation (MPR) processes. Both steady-state and time-resolved measurements are reported and quantitatively explained using the same set of parameters. At higher dopant concentrations (>1% Eu^{3+}), cross-relaxation processes start to contribute to $^5D_1$–$^5D_0$ equilibration and the temperature-dependent luminescence can be explained by including an extra term to account for cross relaxation. The present study provides fundamental insight into thermal equilibration processes in the promising class of Ln-doped temperature sensors. The present work is focused on $NaYF_4$:Eu^{3+}, but the model and conclusions are valid for other Ln-based (nano)thermometers. A better insight into the non-Boltzmann behavior and the use of dopant concentration to extend the effective temperature range are important in the application of luminescence thermometry for remote temperature sensing.

II. Eu^{3+} EMISSION IN $NaYF_4$

We first assess to what extent Boltzmann equilibration is established. To this end, the temperature dependence of the $^5D_1$ and $^5D_0$ [Fig. 1(a)] Eu^{3+} luminescence in $NaYF_4$ for a low-dopant concentration (0.4% Eu^{3+}) is studied to characterize the temperature-dependent emission for Eu^{3+} ions that are isolated from one another. Emission spectra are recorded at different temperatures between 300 and 900 K (from black to orange) with intervals of 25 K as shown in Fig. 1(b). Following excitation in the $^5L_6$ state at 395 nm, the system relaxes to the $^5D_1$ and $^5D_0$ states (indexed throughout with 2 and 1, respectively) whose characteristic luminescences can be observed around 530 nm ($^5D_1$–$^7F_1$) and 615 nm ($^5D_0$–$^7F_2$).

In the case where the $^5D_1$ and $^5D_0$ states are strongly coupled through fast equilibration, their populations, N_2 and N_1, follow Boltzmann statistics:

$$\frac{N_2}{N_1} = \frac{g_2}{g_1}\exp(-\Delta E/kT), \tag{1}$$

in which g_1 and g_2 are the level multiplicities. Toward higher temperatures, the ratio N_2/N_1 then would increase and so would the luminescence intensity of the $^5D_1$–^7F_J ($J = 0$–6) transitions relative to the $^5D_0$–^7F_J transitions. Instead, we initially observe the opposite, a decrease of the relative $^5D_1$ emission intensity, indicating that the conditions for Boltzmann equilibrium are not met.

To make this more quantitative, luminescence intensities are calculated by integrating the total luminescence intensity between 548–586 nm (I_2, mainly $^5D_1$ emission) and 586–640 nm (I_1, mainly $^5D_0$ emission). The ratio of I_2/I_1 is plotted logarithmically vs the reciprocal temperature $1/T$ in Fig. 1(c). Emission intensity scales linearly with the population of an emitting state. This results in an expected (Boltzmann) temperature dependence of the

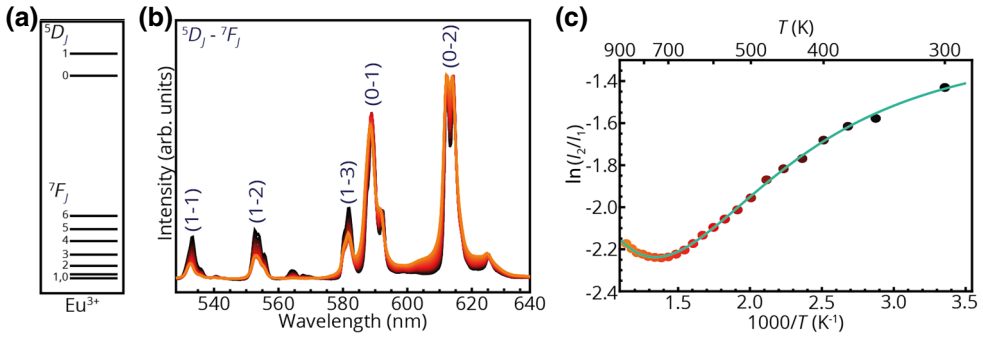

FIG. 1. Emission spectra of $NaYF_4:Eu^{3+}$ (0.4%) upon excitation at 395 nm taken at different temperatures ranging from 300 K (black) to 900 K (orange) with ^5D_J–^7F_J transitions (a) labeled by the J numbers between brackets (b). The ratio between the integrated emission peaks originating from the $^5D_0$ and $^5D_1$ peaks are plotted vs $1000/T$ (c). The cyan line is a fit as discussed in Sec. V.

luminescence intensity ratio given by:

$$\frac{I_2}{I_1} = \frac{A_2 h\nu_2 N_2}{A_1 h\nu_1 N_1} = \exp(-\Delta E/kT). \tag{2}$$

Here, A_i is the spontaneous emission rate and ν_i is the frequency of the transition from state i to the ground state. The temperature-independent constant C accounts for differences in emission rates of luminescence transitions, the restrictions in the integration boundaries in the spectrum [cf. Fig. 1(c)], and any residual optical dispersion. The constant C is around 0.5, as determined from fits to theory as presented below. By plotting the logarithm of the luminescence intensity ratio vs reciprocal temperature, a linear downward trend should be observed. Clearly, for $NaYF_4:Eu^{3+}$ 0.4%, this is not observed. Only above approximately 700 K ($1000/T < 1.4$ K^{-1}) is the expected trend apparent, showing that the luminescence intensity ratio of $^5D_1$ and $^5D_0$ emission fails to satisfy Boltzmann statistics below 700 K.

III. MODEL

To understand and model the observed temperature-dependent luminescence, the populations N_1 of the $^5D_0$ and N_2 of the $^5D_1$ state are evaluated as they evolve over time at a given temperature. The populations are governed by feeding optical pumping into an even higher state, subsequent relaxation (α and β) to the $^5D_1$ and $^5D_0$ states, the radiative decay rates from these states to the ^7F multiplet (τ_2 and τ_1), phonon-induced relaxation processes connecting the $^5D_1$ and $^5D_0$ excited states, and at higher concentrations of Eu^{3+} (see Sec. VI), cross relaxation (X_1 and X_2). The various processes are depicted in Fig. 2. Bridging the energy gap ΔE between $4f^6$ states of an isolated Eu^{3+} ion generally has to occur via phonon emission and phonon absorption, which is known as MPR. The number of phonons that is needed to bridge the gap is p and is determined by dividing the energy gap ΔE by the maximum energy of vibrations (phonons) in the lattice [34]. MPR can be viewed as resonant energy transfer to a resonant overtone vibration in the host lattice or a combination of different phonons to bridge the gap between the $^5D_1$ and $^5D_0$ states. Multiphonon relaxation has been studied in the past in pioneering work by Riseberg and Moos [35] and Layne, Lowdermilk, and Weber [36]. The energy gap ΔE between the $^5D_1$ and $^5D_0$ states is ca. 1800 cm^{-1} as calculated from the $^5D_1$–$^7F_1$ and $^5D_0$–$^7F_1$ emission peak positions from Fig. 1. Since the maximum phonon energy in fluorides is ca. 500 cm^{-1}, it is expected that around four phonons are involved in MPR between the $^5D_1$ and $^5D_0$ excited states. Cross relaxation involves partial energy

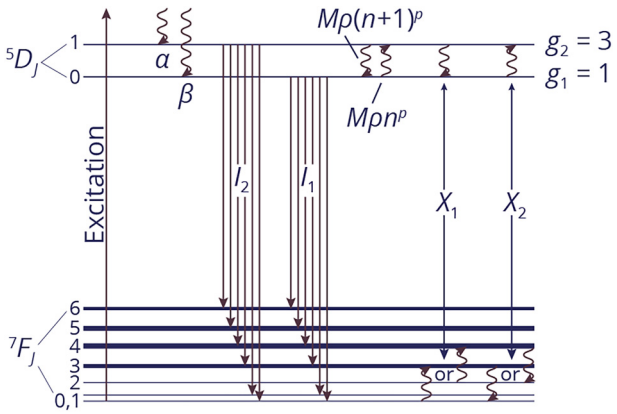

FIG. 2. Excited-state dynamics upon excitation in $^5L_6$ energy level at 395 nm. The processes that determine excited-state populations are excitation, direct relaxation to $^5D_1$ and $^5D_0$ levels with a degeneracy of g_2 and g_1, (α and β, respectively), $^5D_1$–^7F_J and $^5D_0$–^7F_J emission (I_2 and I_1, respectively), multiphonon relaxation from the $^5D_1$ to the $^5D_0$ level (Mpg_2n^p) and from the $^5D_0$ to the $^5D_1$ level [$Mpg_1(1+n)^p$], and finally, cross relaxation from the $^5D_1$ to the $^5D_0$ level (X_1) and from the $^5D_0$ to the $^5D_1$ level (X_2).

transfer between neighboring ions. For Eu^{3+}, this can occur due to the similar energy difference between the $^5D_1$ and $^5D_0$ excited states and the $^7F_0$ and $^7F_3$ ground states. An Eu^{3+} ion can relax from the $^5D_1$ excited state to the $^5D_0$ excited state by transferring the excess energy to a second Eu^{3+}, which is excited from the $^7F_0$ to the $^7F_3$ level or vice versa. At elevated temperatures, as higher-energy ^7F levels are thermally populated, additional cross-relaxation processes may contribute as well.

To evaluate the excited-state populations, differential equations for the populations of the $^5D_0$ and $^5D_1$ states (N_1 and N_2) are considered:

$$\frac{dN_1}{dt} = \beta N^* - \frac{N_1}{\tau_1} + M\rho[(1+n)^p g_1 N_2 - n^p g_2 N_1] + X_1 N_2 - X_2 N_1, \quad (3)$$

$$\frac{dN_2}{dt} = \alpha N^* - \frac{N_2}{\tau_2} - M\rho[(1+n)^p g_1 N_2 - n^p g_2 N_1] - X_1 N_2 + X_2 N_1. \quad (4)$$

Here, the first term describes the ratio of feeding N^* into the $^5L_6$ level and the subsequent relaxation to the $^5D_1$ and $^5D_0$ states (β and α, respectively). Here, we assume that all excited ions relax to the $^5D_1$ or $^5D_0$ level, so that $\alpha+\beta=1$. The second term accounts for the radiative relaxation, which depends on the population of the state and the radiative lifetime (τ_i). The third and fourth terms in Eqs. (3) and (4) are of prime importance to the present analysis as they account for the multiphonon-induced relaxation connecting the two emitting states. The final two terms become important at higher dopant concentrations and represent cross-relaxation processes, which depend on the population of the states involved and the effective rate of cross relaxation (X_i) between neighboring Eu^{3+} ions. The multiphonon relaxation rate from the $^5D_1$ to the $^5D_0$ level and vice versa (third and fourth terms) [37] scale with $M\rho$, the product of the net interaction matrix element of the two-level system with the density of phonon states resonant with the two-level system and g_i the degeneracy of state i. The MPR rates depend exponentially on p, the number of phonons needed to bridge the energy gap ΔE. Important for the present analysis is the temperature dependence of the multiphonon relaxation processes. Phonon emission scales with $(n+1)^p$ and phonon absorption with n^p [38], where n is the Bose-Einstein phonon-occupation number, which is defined as [39]

$$n = \frac{1}{\exp(\Delta E/pkT) - 1}. \quad (5)$$

The model presented can be applied to quantitatively model the observed temperature dependence of the emission-intensity ratio under continuous excitation [as shown in Fig. 1(c)]. Note that in Eqs. (3) and (4), degeneracy g_1 of $^5D_0$ comes in combined with N_2, because the system, when residing in a particular sublevel of $^5D_1$ may, in accordance with MPR, relax to each of the g_1 sublevels of $^5D_0$, and similarly g_2 of $^5D_1$ is combined with N_1. Inclusion of g_1 and g_2 in Eqs. (3) and (4) combined with Eq. (5) ensures conformity with Boltzmann statistics in the case of dominant thermal relaxation. In addition, the time dependence of the luminescence intensity for emission from both the $^5D_0$ and $^5D_1$ states can be modeled as a function of temperature and provide information on the temperature dependence of the relaxation rates between the $^5D_0$ and $^5D_1$ levels. Below, we analyze both the temperature-dependent excited-state dynamics and intensity ratio based on Eqs. (3) and (4). First, results for the low Eu^{3+} concentration (0.4%) are considered to obtain information on the parameters for isolated Eu^{3+} ions and then the role of additional relaxation processes by cross-relaxation processes at higher Eu^{3+} concentrations is discussed.

IV. EXCITED-STATE DYNAMICS

Since the population in an excited state is proportional to the luminescence intensity from that state [Eq. (2)], it is possible to validate Eqs. (3) and (4) using luminescence decay measurements. In Fig. 3, the luminescence decay is presented for the $^5D_0$ state upon excitation in $^5D_0$ (panel a) and $^5D_1$ (panel b) as well as for $^5D_1$ emission upon excitation in $^5D_0$ (panel c) and $^5D_1$ (panel d). The panels show decay curves for a series of temperatures starting at 300 K, followed by 373 K to 873 K in 100 K steps (colors varying from dark blue to orange). An exception is panel c, because below 573 K, the emission from $^5D_1$ is too weak for a measurable signal. The data is fitted with a bi-exponential fit for Figs. 3(a)–3(d). The parameters obtained from the fitting are summarized in Tables S1–S4 [40].

Upon excitation in the $^5D_0$ state, the $^5D_0$ emission intensity decays bi-exponentially for all temperatures with an initial fast decay time and a subsequent lifetime of ca. 6 ms [Fig. 3(a)], comparable to radiative lifetimes for Eu^{3+} $^5D_0$ emission in $NaYF_4$ found in other works [31,41]. Similar lifetimes are found upon excitation in the $^5D_1$ state in addition to an initial rise time, which become faster with increasing temperature. In the case of a significant contribution from cross relaxation between an Eu^{3+} ion in the $^5D_0$ excited state and a neighboring ion in the $^7F_3$ ground state, multi-exponential decay is expected based on the random distribution of the ions in the lattice. However, this multi-exponential decay is not observed, and therefore, cross relaxation (X_2) is negligible, as expected for systems with such a low-dopant concentration [42].

The $^5D_1$ emission for $^5D_0$ excitation, shown in Fig. 3(c), shows an initial rise and a subsequent decay in intensity. The long decay lifetime is comparable to the radiative

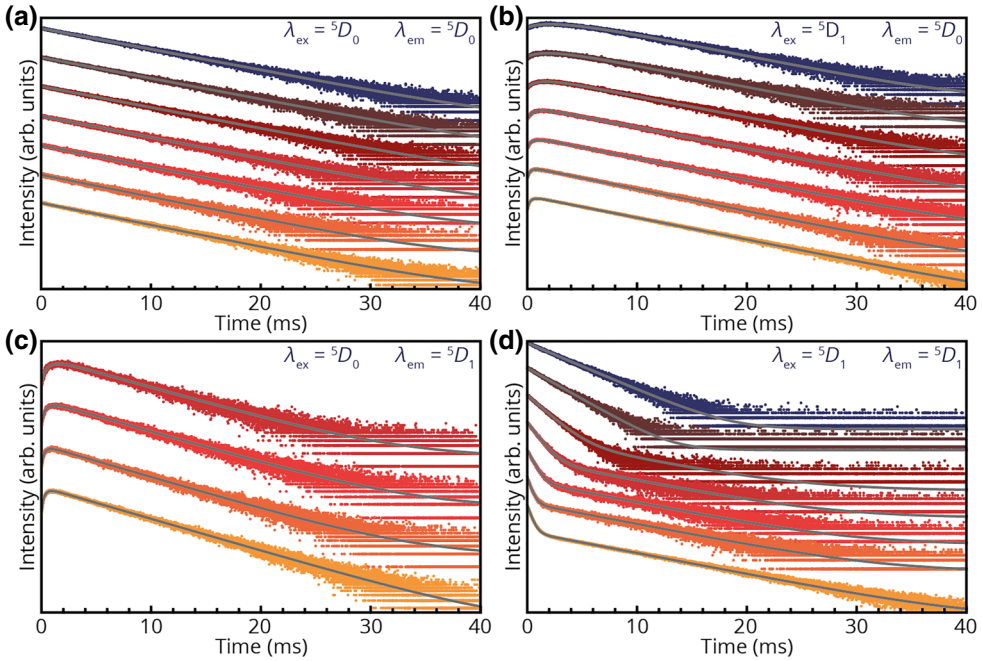

FIG. 3. Luminescence decay measurements in $NaYF_4:Eu^{3+}$ (0.4%) at temperatures ranging from 300 K (dark blue) to 900 K (orange) while exciting in the ${}^5D_0$ and ${}^5D_1$ states and monitoring the ${}^5D_0$ level (a and b, respectively) and while exciting in the ${}^5D_0$ and ${}^5D_1$ levels and monitoring the ${}^5D_1$ level (c and d, respectively). Biexponential fits are shown in gray.

lifetimes of the ${}^5D_0$ state. Again, the initial rise becomes faster with increasing temperature. Upon direct excitation in the ${}^5D_1$ level, as shown in Fig. 3(d), a fast, temperature-dependent decay is observed and a longer decay component is observed for temperatures higher than 473 K. The long component has a lifetime of ca. 6 ms and the fast component shows the same temperature dependency as the rise time in Fig. 3(b). Consequently, the short component is attributed to fast initial ${}^5D_1$–${}^5D_0$ decay. In the case of cross relaxation between an ion in the ${}^5D_1$ excited state and an ion in the ${}^7F$ ground multiplet, this fast component is expected to be multi-exponential as a result of a variation in cross-relaxation rates for different local environments (variations in distances to neighboring Eu^{3+} ions). Since the fast component is of mono-exponential nature, cross relaxation from the ${}^5D_1$ excited state (X_1) is not observed, as expected for systems with a low 0.4% dopant concentration homogeneously distributed in the host lattice.

For a precise analysis of the decays in Fig. 3, we apply the model developed in Sec. III. The differential Eqs. (3) and (4) can be solved analytically to obtain N_1 and N_2 vs time. The resulting expression can be simplified because radiative lifetimes from the ${}^5D_0$ and the ${}^5D_1$ states are both ca. 6 ms and because of this coincidental similarity, we can replace τ_1 and τ_2 in Eqs. (3) and (4) with τ_R. Upon ignoring cross relaxation ($X_1 = X_2 = 0$), the solution becomes

$$N_1 = C_1 \exp(-r_1 t) + \frac{g_1(1+n)^p}{g_2 n^p} C_2 \exp(-r_2 t), \quad (6)$$

$$N_2 = C_1 \exp(-r_1 t) + C_2 \exp(-r_2 t), \quad (7)$$

in which C_1 and C_2 are integration constants and the decay rates r_1 and r_2 are defined as

$$r_1 = \frac{1}{\tau_R} + \frac{1}{\tau_{NR}}, \quad (8)$$

$$r_2 = \frac{1}{\tau_R}, \quad (9)$$

with $1/\tau_{NR}$ defined as

$$\frac{1}{\tau_{NR}} = M\rho[g_1(1+n)^p + g_2 n^p]. \quad (10)$$

Fitting Eqs. (6) and (7) to each set of decay curves in Fig. 3 yields the decay rates r_1 and r_2, which can be rewritten as τ_R and τ_{NR} using Eqs. (8) and (9). The resulting values of τ_R and τ_{NR} are plotted vs the temperature in Fig. 4 for the four different sets of temperature-dependent decay curves [${}^5D_0$ emission upon excitation in the ${}^5D_0$ and ${}^5D_1$ (blue and red) and ${}^5D_1$ emission upon excitation in the ${}^5D_1$ and ${}^5D_0$ (orange and green)] and collected in Tables S1–S4 of the Supplemental Material [40].

The agreement between the temperature-dependent values for τ_R and τ_{NR} from the four different sets of decay curves is good. The radiative decay times are at first approximation temperature independent, but do show a small decrease with temperature (approximately 7% decrease from 300–900 K), which is explained by a small increase of the radiative transition probability for vibrationally induced forced electric-dipole transitions (increases with $2n+1$) [43,44]. The nonradiative decay time shows a much stronger decrease with temperature

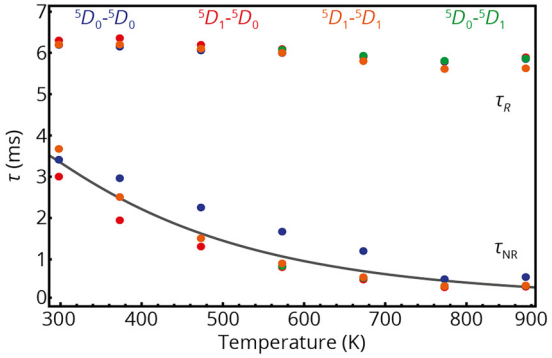

FIG. 4. Values of τ_R and τ_{NR} as function of temperature as obtained from the fits in Fig. 3 and calculated using Eqs. (8) and (9). The gray fit through the τ_{NR} values is according to Eq. (10) and yields $M\rho = 0.22 \pm 0.03$ ms^{-1} and $p = 3.7 \pm 0.2$.

and closely follows the theoretically expected temperature dependence [Eq. (10), gray curve]. The parameters for the fit, $M\rho$ and p are 0.22 ± 0.03 ms^{-1} and 3.7 ± 0.2, respectively. Since the maximum phonon energy in fluoride lattices is ca. 500 cm^{-1} and the energy gap between the $^5D_1$ and $^5D_0$ excited states is ca. 1800 cm^{-1}, the number of phonons needed to bridge the energy gap, p, is in good agreement with the expected results. The good fit indicates that the theory for multiphonon relaxation adequately describes the temperature dependence of the decay dynamics for Eu^{3+} emission in $NaYF_4$. The fit parameters and Eqs. (3) and (4) can now be used to obtain an expression for I_2/I_1 and fit the results for the measured temperature dependence of the steady-state intensity ratio shown in Fig. 1(b).

V. STEADY-STATE MEASUREMENTS

Temperature-dependent luminescence as shown in Fig. 1 is measured under cw excitation in the $^5L_6$ level. Under cw excitation, the system reaches a steady state and the population in the excited states N_1 and N_2 is constant in time ($dN_1/dt = 0$ and $dN_2/dt = 0$). Under these conditions, Eqs. (3) and (4) can be solved, in the absence of cross relaxation, resulting in

$$\frac{I_2}{I_1} = C\frac{(\alpha/\tau_R) + M\rho g_2 n^p}{(\beta/\tau_R) + M\rho g_1 (1+n)^p}. \tag{11}$$

Equation (11) is fitted to the data in Fig. 1(c) (cyan line). The fit is in good agreement with the obtained values for I_2/I_1 over the full range of temperatures with fitting parameters $C = 0.45 \pm 0.02$, $\alpha = 0.77 \pm 0.08$, $\beta = 0.23 \pm 0.08$, $M\rho = 0.17 \pm 0.03$ ms^{-1}, and $p = 3.63 \pm 0.15$. The fitting parameter C correlates N_2/N_1 and I_2/I_1, as I_2 and I_1 are intensities integrated over only a part of the total luminescence from the $^5D_0$ and $^5D_1$ in the emission spectra (Fig. 1). The time τ_R, needed in these fits, is determined by averaging the long-lifetime components of Fig. 4 with the result of 6.0 ± 0.1 ms. The fractions α and β, which govern the feeding fraction of the $^5D_1$ and $^5D_0$ levels, respectively, are consistent with expectations: relaxation from the $^5L_6$ excited state to the $^5D_1$ and $^5D_0$ states goes via multiple steps, resulting in a more efficient relaxation to the higher energy $^5D_1$ state compared to the $^5D_0$ state.

The value of $M\rho$, 0.17 ms^{-1}, closely matches the value of $M\rho$ determined from the excited-state dynamics, 0.22 ms^{-1}. The p values (number of phonons involved in the $^5D_1$ to $^5D_0$ MPR) obtained from the time-resolved and steady-state measurements, 3.7 and 3.63, are in good agreement and are consistent with the maximum phonon energy in fluorides (approximately 500 cm^{-1}) and the energy difference between the $^5D_1$ and $^5D_0$ states (approximately 1800 cm^{-1}).

In summary of Secs. IV and V, the temperature dependence of both time-resolved and stationary-state measurements are consistently accounted for by the model presented in Sec. III based on pure multiphonon relaxation between $^5D_1$ and $^5D_0$ states. In addition, we establish that phonon bottlenecking of zone-boundary phonons [45] is absent by measuring luminescence decay at different excitation powers. In the case of phonon bottlenecking, a limited number of available phonons influences the relaxation process resulting in slower equilibration between the $^5D_1$ and $^5D_0$ states. However, time-resolved luminescence measurements show no difference when varying the excitation power, indicating that phonon bottlenecking is not present (data not shown here). The model of Sec. III is also extended by incorporation of Raman relaxation processes, but this did not improve the fits. The fact that the temperature-dependent properties for time-resolved and steady-state measurements can be explained using the same parameters indicates that the multiphonon relaxation model accurately describes the relaxation processes between the $^5D_1$ and $^5D_0$ levels.

Interestingly, the results show that even at the highest temperatures probed, a true Boltzmann equilibrium is not yet realized for the low-doped 0.4% sample. This is evident from Fig. 1 where the intensity ratio starts to increase toward Boltzmann equilibrium only between 700 and 900 K. Between 300 K and 700 K, the intensity ratio decreases while an increase of the ratio would be expected based on Boltzmann statistics predicting a higher $^5D_1$ population at higher temperatures. Conclusive evidence is obtained from the time-resolved data. These show that even at 900 K, bi-exponential decay curves are observed. For a true Boltzmann equilibrium where relaxation rates between two thermally coupled levels are much faster than radiative decay, a single exponential decay is expected that is identical for emission from both levels. Clearly, for Eu^{3+}, this has not been realized at 900 K. In general, it is important to verify the validity of a Boltzmann equilibrium in luminescence thermometry

when temperature-dependent data and calibration curves are based on Boltzmann statistics. In the past, this has not always been the case [18–20], especially for ratiometric analysis relying on emission from states separated by a larger ΔE, as for example, in Dy^{3+} and Eu^{3+}. Deviations from Boltzmann behavior sometimes go unnoticed or are not explained correctly [18–20]. The present analysis shows that the temperature dependence of the emission intensity ratio outside the Boltzmann regime can be accurately modeled and used to understand and predict deviations from Boltzmann behavior.

VI. CROSS-RELAXATION

To extend the temperature range for luminescence thermometry toward lower temperatures, it is desirable to make the equilibration among the coupled levels faster than MPR allows for levels separated by a large ΔE. A potential mechanism to induce relaxation is cross relaxation (partial energy transfer between neighboring ions). This can be observed for Eu^{3+} at elevated doping levels. At higher concentrations of Eu^{3+}, the distance between Eu^{3+} neighbors decreases and the effect of the cross relaxation becomes important. For Eu^{3+}, cross relaxation can occur as the energy difference between the $^5D_0$ and $^5D_1$ excited states and the $^7F_0$ and $^7F_3$ ground states is similar. The $^5D_1$–$^5D_0$ energy can be transferred to a neighboring Eu^{3+} in the $^7F_0$ ground state that is raised to the $^7F_3$ state. There is a small energy mismatch between the $^5D_0$–$^5D_1$ and $^7F_0$–$^7F_3$ gaps and the small energy mismatch can be overcome by emission or absorption of low-energy phonons.

The cross-relaxation rates depend on the distribution of Eu^{3+} ions. As a result, every Eu^{3+} with a unique distribution of Eu^{3+} neighbors gives rise to a unique relaxation pathway. Subsequently, the average relaxation time of an ensemble of Eu^{3+} ions is governed by the distribution of configurations resulting in a multi-exponential decay during time-resolved luminescence as shown in Figs. S3 and S4 for samples with Eu^{3+} concentrations of 5.5% and 8.4%, respectively [46]. The time-resolved luminescence measurements cannot be fitted properly with a simple model with a fixed value for cross-relaxation rates X_1 and X_2 because of different configurations of the Eu^{3+} ions in the lattice, and indeed a clear deviation from single-exponential behavior is observed for the rise and initial decay part of the luminescence decay curves for the 5.5% and 8.4% Eu-doped samples.

Stationary-state measurements, on the other hand, have the virtue of integrating the decays over time. The temporal dependences of the various relaxation processes are thus integrated out. To explore the effect of the Eu^{3+} concentration on the temperature-dependent $^5D_1/^5D_0$ intensity ratio, the luminescence of two samples with higher Eu^{3+} concentrations of 5.5% and 8.4% has been measured. The results

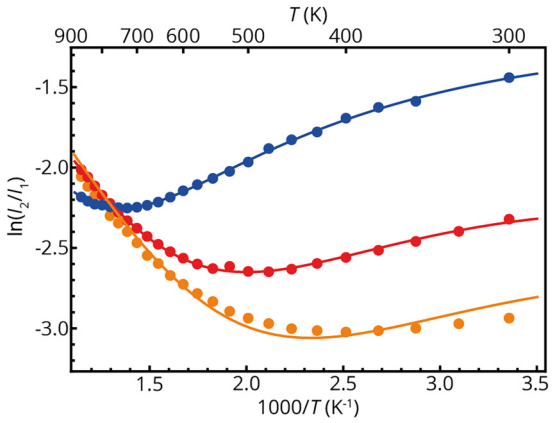

FIG. 5. Log of the luminescence intensity ratio plotted vs $1000/T$ for the samples with Eu^{3+} concentrations of 0.4% (blue), 5.5% (red), and 8.4% (orange). The curves are fits of Eq. (11) to the 0.4% data in Sec. V, and of Eq. (12) with Eqs. (S1), (S2), and (S3) inserted for the 5.5% and 8.4% data [46].

(colored red and orange) are presented in Fig. 5 in comparison with the results for 0.4% (colored blue) duplicated from Fig. 1(c).

We can rewrite Eq. (11) to include the temperature-dependent cross-relaxation processes, resulting in

$$\frac{I_2}{I_1} = C\frac{(\alpha/\tau_R) + M\rho g_2 n^p + X_2}{(\beta/\tau_R) + M\rho g_1(1+n)^p + X_1}. \qquad (12)$$

Here, X_1 and X_2 are the cross-relaxation terms for the $^5D_1$–$^5D_0$ and $^5D_0$–$^5D_1$ relaxations, respectively. The modeling is furthermore made to include the transition connecting the $^7F_2$ and $^7F_4$ levels, which involves approximately the same energy (ca. 1800 cm^{-1}), and indeed contributes significantly at elevated temperatures. The thermal populations of the $^7F_2$ and $^7F_4$ are admittedly smaller, but the transition matrix elements connecting them are significantly larger, because $\Delta J = \pm 2$ as compared to $\Delta J = \pm 3$.

To test the influence of Eu^{3+} concentration on the temperature-dependent $^5D_1/^5D_0$ intensity ratio, Eq. (12) is fitted to the temperature-dependent luminescence of two samples with higher Eu^{3+}-dopant concentrations, 5.5% and 8.4% [46]. It is evident that the temperature dependence of the intensity ratio is strongly influenced by the Eu^{3+} concentration. For a higher concentration, the ratio I_2/I_1 is much lower at room temperature as a result of faster $^5D_1$–$^5D_0$ relaxation and the temperature-dependent $^5D_1/^5D_0$ intensity ratio can be used to probe temperatures above ca. 500 K.

The analysis of the concentration dependence of the intensity ratio shows that the useful temperature range for luminescence thermometry can be controlled and extended through the dopant concentration. It also reveals that the dopant concentration is an important parameter in the evaluation of the performance of (nano)thermometers based

on Ln-doped luminescent materials and the temperature regime in which a Boltzmann equilibrium is reached. The obtained relative sensitivities/temperature uncertainties are 0.05% K^{-1}/50.0 K, 0.09% K^{-1}/23.9 K, and 0.12% K^{-1}/19.2 K for the 0.4%, 5.5%, and 8.4% samples, respectively.

Implications of the present analysis are schematically depicted in Fig. 6 for Eu^{3+} as well as two other lanthanide ions (Er^{3+} and Dy^{3+}) commonly used for luminescence thermometry. Three different temperature regimes can be discerned: nonradiative relaxation much faster than radiative decay (Boltzmann regime, left-hand side), nonradiative and radiative decay rates are similar (middle), and radiative decay faster than nonradiative decay (right-hand side). For the latter two regimes, the temperature dependence of the emission intensity ratio I_2/I_1 does not follow Boltzmann statistics. The relative intensity of the upper level I_2 can even decrease with increasing temperature, opposite to what is expected from Boltzmann statistics. The regime that is applicable strongly depends on the energy gap ΔE between the thermally coupled levels. The lines at the bottom mark the valid regime (300–900 K) for the three ions, where the starting point at the right-hand side of the line marks room temperature. The schematic shows that for Er^{3+} with the smallest ΔE (approximately 700 cm^{-1} for $^2H_{11/2}$–$^4S_{3/2}$), the Boltzmann behavior already starts below room temperature. For Dy^{3+} with a larger ΔE (approximately 1000 cm^{-1} for $^4I_{15/2}$–$^4F_{9/2}$), Boltzmann behavior is realized at temperatures higher than room temperature but well below 900 K. For Eu^{3+} with the largest ΔE (approximately 1800 cm^{-1} for $^5D_1$–$^5D_0$),

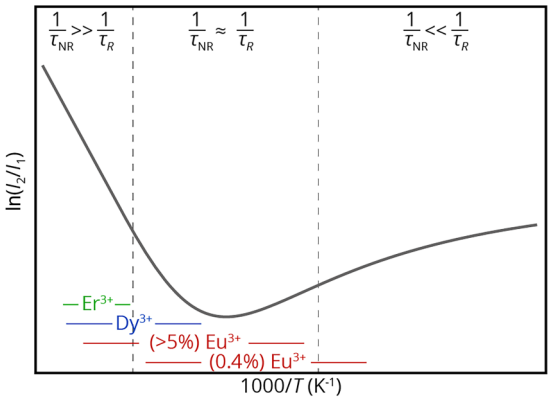

FIG. 6. Fluorescence intensity ratio plotted vs $1/T$ for three Ln ions commonly used in luminescence thermometry. The energy gap ΔE between the thermally coupled levels increases from Er^{3+} to Dy^{3+} to Eu^{3+}. The drawn lines at the bottom indicate the temperature regimes that apply to these ions. In the case of $1/\tau_{NR} \ll 1/\tau_R$, the FIR will decrease with increasing temperature (right-hand side), in the case of $1/\tau_{NR} \approx 1/\tau_R$, there is a local minimum in the FIR (middle) and in the case of $1/\tau_{NR} \gg 1/\tau_R$, Boltzmann behavior determines an increase of FIR with increasing T (left-hand side).

Boltzmann equilibrium is not realized even at the highest temperatures investigated in this study (900 K). However, by introducing additional relaxation pathways, e.g., through cross relaxation at higher Eu^{3+} concentrations, the temperature regime for luminescence thermometry can be shifted toward lower temperatures. The present analysis shows that the validity of Boltzmann statistics needs to be considered in the application of luminescence thermometry based on both ΔE [Eu^{3+}– (this work), compared to Dy^{3+}-doped samples [18,19,47,48] and Er^{3+}-doped samples [17,26–28,49]] and the dopant concentration (Fig. 5). For example, in our work [Fig. 1(c)], a deviation from Boltzmann behavior can be observed for all measured temperatures (300–900 K), a deviation from Boltzmann behavior can be observed from 300–500 K in ref. [47] for Dy^{3+}, and finally, a deviation from Boltzmann behavior can be observed above 800 K in [17] for Er^{3+}.

VII. CONCLUSIONS

To investigate the validity of Boltzmann equilibrium in Ln-based luminescence thermometry, the temperature dependence of the $^5D_1$ and $^5D_0$ emissions of Eu^{3+} in $NaYF_4$ is investigated between 300 and 900 K. Both steady-state and time-resolved luminescence spectroscopy experiments are reported for three different Eu^{3+} concentrations (0.4%, 5.5%, and 8.4%). For 0.4% doping, all decay curves for $^5D_1$ and $^5D_0$ emissions (upon both $^5D_1$ and $^5D_0$ excitation) show a consistent behavior that can be explained by $^5D_1$–$^5D_0$ and, at higher temperatures, $^5D_0$–$^5D_1$ multiphonon relaxation. Upon raising the temperature, relaxation rates increase as predicted by theoretical models for multiphonon relaxation. The temperature dependence measured for the $^5D_1/^5D_0$ emission intensity ratio is in good quantitative agreement with the relaxation parameters determined from the temperature-dependent emission decay curves. The results reveal that even at the highest temperatures (up to 900 K), relaxation between the $^5D_0$ and $^5D_1$ levels is not fast enough to establish Boltzmann equilibrium. This limits the temperature range in which $NaYF_4$:Eu^{3+} can be used for ratiometric luminescence thermometry. To extend the temperature range, faster $^5D_1$–$^5D_0$ relaxation can be realized by increasing the Eu^{3+}-doping concentration to induce cross relaxation between Eu^{3+} neighbors. Modelling of the temperature-dependent luminescence intensity ratio indicates that both $^5D_1$–$^5D_0$ to $^7F_0$–$^7F_3$ and $^5D_1$–$^5D_0$ to $^7F_2$–$^7F_4$ cross relaxations contribute.

The present study gives insight into processes that determine equilibration between thermally coupled levels of Ln emitters used in ratiometric luminescence thermometry. Upon increasing the energy difference ΔE between levels, which is required for accurate sensing of high temperatures, relaxation rates decrease and deviations from Boltzmann equilibrium occur in the lower temperature regime.

Models for the temperature dependence of multiphonon relaxation rates can be used to quantitatively model the temperature dependence and give insight into the practical temperature range. The temperature range can be optimized by varying the Ln-dopant concentration to enhance relaxation rates through cross relaxation. In the development of Ln-based luminescent (nano)thermometers, it is important to evaluate the validity of Boltzmann equilibration and understand deviations from Boltzmann behavior to extend and improve the accuracy of temperature calibration curves.

ACKNOWLEDGMENTS

O. L. J. Gijzeman is gratefully acknowledged for the scientific discussions. This work was supported by the Netherlands Center for Multiscale Catalytic Energy Conversion (MCEC), an NWO Gravitation program funded by the Ministry of Education, Culture and Science of the government of the Netherlands.

[1] D. Jaque and F. Vetrone, Luminescence nanothermometry, Nanoscale **4**, 4301 (2012).

[2] H. Kusama, O. J. Sovers, and T. Yoshioka, Line shift method for phosphor temperature measurements, Jpn. J. Appl. Phys. **15**, 2349 (1976).

[3] L. D. Carlos and F. Palacio, *Thermometry at the Nanoscale: Techniques and Selected Applications* (RSC Publishing, Cambridge, 2015).

[4] B. del Rosal, E. Ximendes, U. Rocha, and D. Jaque, In vivo luminescence nanothermometry: From materials to applications, Adv. Opt. Mater. **5**, 1600508 (2017).

[5] F. Vetrone, R. Naccache, A. Zamarrón, A. J. de la Fuente, F. Sanz-Rodríguez, L. M. Maestro, E. M. Rodriguez, D. Jaque, J. G. Solé, and J. A. Capobianco, Temperature sensing using fluorescent nanothermometers, ACS Nano **4**, 3254 (2010).

[6] J. M. Yang, H. Yang, and L. Lin, Quantum dot nano thermometers reveal heterogeneous local thermogenesis in living cells, ACS Nano **5**, 5067 (2011).

[7] C. Gota, K. Okabe, T. Funatsu, Y. Harada, and S. Uchiyama, Hydrophilic fluorescent nanogel thermometer for intracellular thermometry, J. Am. Chem. Soc. **131**, 2766 (2009).

[8] M. Xu, X. Zou, Q. Su, W. Yuan, C. Cao, Q. Wang, X. Zhu, W. Feng, and F. Li, Ratiometric nanothermometer in vivo based on triplet sensitized upconversion, Nat. Commun. **9**, 2698 (2018).

[9] S. Kalytchuk, K. Poláková, Y. Wang, J. P. Froning, K. Cepe, A. L. Rogach, and R. Zbořil, Carbon dot nanothermometry: Intracellular photoluminescence lifetime thermal sensing, ACS Nano **11**, 1432 (2017).

[10] L. Aigouy, G. Tessier, M. Mortier, and B. Charlot, Scanning thermal imaging of microelectronic circuits with a fluorescent nanoprobe, Appl. Phys. Lett. **87**, 1 (2005).

[11] A. Bar-Cohen and P. Wang, On-chip hot spot remediation with miniaturized thermoelectric coolers, Microgravity Sci. Technol. **21**, 351 (2009).

[12] M. L. Toebes, F. F. Prinsloo, J. H. Bitter, A. J. van Dillen and K. P. de Jong, Influence of oxygen-containing surface groups on the activity and selectivity of carbon nanofiber-supported ruthenium catalysts in the hydrogenation of cinnamaldehyde, J. Catal. **214**, 78 (2003).

[13] J. D. Grunwaldt, J. B. Wagner, and R. E. Dunin-Borkowski, Imaging catalysts at work: A hierarchical approach from the macro- to the meso- and nano-scale, ChemCatChem. **5**, 62 (2013).

[14] E. Borodina, F. Meirer, I. Lezcano-González, M. Mokhtar, A. M. Asiri, S. A. Al-Thabaiti, S. N. Basahel, J. Ruiz-Martinez, and B. M. Weckhuysen, Influence of the reaction temperature on the nature of the active and deactivating species during methanol to olefins conversion over H-SSZ-13, ACS Catal. **5**, 992 (2015).

[15] R. G. Geitenbeek, A.-E. Nieuwelink, T. S. Jacobs, B. B. V. Salzmann, J. Goetze, A. Meijerink, and B. M. Weckhuysen, In situ luminescence thermometry to locally measure temperature gradients during catalytic reactions, ACS Catal. **8**, 2397 (2018).

[16] C. D. S. Brites, P. P. Lima, N. J. O. Silva, A. Millán, V. S. Amaral, F. Palacio, and L. D. Carlos, Thermometry at the nanoscale, Nanoscale **4**, 4799 (2012).

[17] R. G. Geitenbeek, P. T. Prins, W. Albrecht, A. van Blaaderen, B. M. Weckhuysen, and A. Meijerink, $NaYF_4:Er^{3+},Yb^{3+}/SiO_2$ core/shell upconverting nanocrystals for luminescence thermometry up to 900 K, J. Phys. Chem. C **121**, 3503 (2017).

[18] S. Ćulubrk, V. Lojpur, S. P. Ahrenkiel, J. M. Nedeljković, and M. D. Dramićanin, Non-contact thermometry with Dy^{3+} doped Gd2Ti2O7 nano-powders, J. Lumin. **170**, 395 (2016).

[19] Z. Cao, S. Zhou, G. Jiang, Y. Chen, C. Duan, and M. Yin, Temperature dependent luminescence of Dy^{3+} doped $BaYF_5$ nanoparticles for optical thermometry, Curr. Appl. Phys. **14**, 1067 (2014).

[20] V. Lojpur, S. Ćulubrk, and M. D. Dramićanin, Ratiometric luminescence thermometry with different combinations of emissions from Eu^{3+} doped $Gd_2Ti_2O_7$ nanoparticles, J. Lumin. **169**, 534 (2016).

[21] W. T. Carnall, H. Crosswhite, and H. M. Crosswhite, *Energy level structure and transition probabilities of the trivalent lanthanides in* LaF_3 (Argonne National Laboratory, Argonne, 1977).

[22] Y. Zhao, C. Riemersma, F. Pietra, R. Koole, C. de Mello Donegá, and A. Meijerink, High-temperature luminescence quenching of colloidal quantum dots, ACS Nano **6**, 9058 (2012).

[23] A. G. Viveros-Andrade, R. Colorado-Peralta, M. Flores-Alamo, S. E. Castillo-Blum, J. Durán-Hernández, and J. M. Rivera, Solvothermal synthesis and spectroscopic characterization of three lanthanide complexes with high luminescent properties $[H_2NMe_2]_3[Ln(III)(2,6\text{-pyridinedicarboxylate})_3]$ (Ln = Sm, Eu, Tb): In the presence of 4,4′-Bipyridyl, J. Mol. Struct. **1145**, 10 (2017).

[24] T. Kissel, J. Brübach, M. Euler, M. Frotscher, C. Litterscheid, B. Albert, and A. Dreizler, Phosphor thermometry: On the synthesis and characterisation of

$Y_3Al_5O_{12}$:Eu (YAG:Eu) and $YAlO_3$:Eu (YAP:Eu), Mater. Chem. Phys. **140**, 435 (2013).

[25] S. W. Allison and G. T. Gillies, Remote thermometry with thermographic phosphors: Instrumentation and applications, Rev. Sci. Instrum. **68**, 2615 (1997).

[26] X. Xu, Z. Wang, P. Lei, Y. Yu, S. Yao, S. Song, X. Liu, Y. Su, L. Dong, J. Feng, and H. Zhang, α-NaYb(Mn)F_4:Er^{3+}/Tm^{3+}@$NaYF_4$ UCNPs as "Band-Shape" luminescent nanothermometers over a wide temperature range, ACS Appl. Mater. Interfaces **7**, 20813 (2015).

[27] M. A. R. C. Alencar, G. S. Maciel, C. B. Araújo, and A. Patra, Er^{3+}-doped $BaTiO_3$ nanocrystals for thermometry: Influence of nanoenvironment on the sensitivity of a fluorescence based temperature sensor, Appl. Phys. Lett. **84**, 4753 (2004).

[28] P. Haro-González, I. R. Martín, L. L. Martín, S. F. Léon-Luis, C. Pérez-Rodríguez, and V. Lavín, Characterization of Er^{3+} and Nd3+ doped Strontium Barium Niobate glass ceramic as temperature sensors, Opt. Mater. **33**, 742 (2011).

[29] L. Đačanin Far, S. R. Lukić-Petrović, V. Đorđević, K. Vuković, E. Glais, B. Viana, and M. D. Dramićanin, Luminescence temperature sensing in visible and NIR spectral range using Dy^{3+} and Nd^{3+} doped $YNbO_4$, Sens. Actuators, A Phys. **270**, 89 (2018).

[30] C. Cao, H. K. Yang, J. W. Chung, B. K. Moon, B. C. Choi, J. H. Jeong, and K. H. Kim, Hydrothermal synthesis and white luminescence of Dy^{3+}-doped $NaYF_4$ microcrystals, J. Am. Ceram. Soc. **94**, 3405 (2011).

[31] C. Li, C. Zhang, Z. Hou, L. Wang, Z. Quan, H. Lian, and J. Lin, β-$NaYF_4$ and β-$NaYF_4$:Eu^{3+} microstructures: Morphology control and tunable luminescence properties, J. Phys. Chem. C **113**, 2332 (2009).

[32] L. Aarts, B. M. van der Ende, and A. Meijerink, Downconversion for solar cells in $NaYF_4$:Er, Yb, J. Appl. Phys. **106**, 023522 (2009).

[33] See Supplemental Material at http://link.aps.org/supplemental/10.1103/PhysRevApplied.10.064006 for methods and structural characterization of the prepared microcrystalline $NaYF_4$.

[34] G. Blasse and B. C. Grabmaier, *Luminescent Materials* (Springer, Berlin, 1994).

[35] L. A. Riseberg and H. W. Moos, Multiphonon orbit-lattice relaxation of excited states of rare-earth ions in crystals, Phys. Rev. **174**, 429 (1968).

[36] C. B. Layne, W. H. Lowdermilk, and M. J. Weber, Multiphonon relaxation of rare-earth ions in oxide glasses, Phys. Rev. B **16**, 10 (1977).

[37] B. Henderson and G. F. Imbusch, *Optical Spectroscopy of Inorganic Solids* (Oxford University Press, Oxford, 2006).

[38] R. Orbach, Spin-lattice relaxation in rare-earth salts, Proc. Roy. Soc. London **A264**, 458 (1961).

[39] S. A. Egorov and J. L. Skinner, On the theory of multiphonon relaxation rates in solids, J. Chem. Phys. **103**, 1533 (1995).

[40] See Supplemental Material at http://link.aps.org/supplemental/10.1103/PhysRevApplied.10.064006 for tables with fitting parameters for the luminescence lifetime experiments of the 0.4% Eu^{3+}-doped $NaYF_4$.

[41] P. Ghosh and A. Patra, Influence of crystal phase and excitation wavelength on luminescence properties of Eu^{3+-}doped sodium yttrium fluoride nanocrystals, J. Phys. Chem. C **112**, 19283 (2008).

[42] D.-C. Yu, R. Martín-Rodríguez, Q.-Y. Zhang, A. Meijerink, and F. T. Rabouw, Multi-photon quantum cutting in Gd_2O_2S:Tm^{3+} to enhance the photo-response of solar cells, Light Sci. Appl. **4**, e344 (2015).

[43] M. Grinberg, $^2E \rightarrow {}^4A_2$ fluorescence of Cr^{3+} in high and intermediate field garnets, J. Lumin. **54**, 369 (1993).

[44] R. J. M. Da Fonseca and T. Abritta, Radiative and nonradiative processes in $LiGa_5O_8$:Mn^{4+}, Phys. B Condens. Matter. **190**, 327 (1993).

[45] H. W. de Wijn, Phonon physics in ruby studied by optical pumping and luminescence, J. Lumin. **125**, 55 (2007).

[46] See Supplemental Material at http://link.aps.org/supplemental/10.1103/PhysRevApplied.10.064006 for more details on the cross-relaxation experiments on the 5.5% and 8.4% Eu^{3+}-doped $NaYF_4$ samples.

[47] L. M. Chepyga, E. Hertle, A. Ali, L. Zigan, A. Osvet, C. J. Brabec, and M. Batentschuk, Synthesis and photoluminescent properties of the Dy^{3+} doped YSO as a high-temperature thermographic phosphor, J. Lumin. **197**, 23 (2018).

[48] E. Hertle, L. Chepyga, M. Batentschuk, S. Will, and L. Zigan, Temperature-dependent luminescence characteristics of Dy^{3+} doped in various crystalline hosts, J. Lumin. **204**, 64 (2018).

[49] P. Du and J. S. Yu, Near-ultraviolet light induced visible emissions in Er^{3+}-activated La_2MoO_6 nanoparticles for solid-state lighting and non-contact thermometry, Chem. Eng. J. **327**, 109 (2017).